Materials Today Communications 29 (2021) 102735

Contents lists available at ScienceDirect

Materials Today Communications

journal homepage: www.elsevier.com/locate/mtcomm

On the optical properties and dynamical and mechanical stability of 1T PdSSe, PdSTe, and PdSeTe monolayers under biaxial strain

W.A. Diery [a], Elie.A. Moujaes [b,*]

[a] Physics Department, Faculty of Science, King AbdulAziz University, 21589 Jedda, Saudi Arabia
[b] Physics Department, Federal University of Rondônia, 76900-900 Porto Velho, Brazil

ARTICLE INFO

Keywords:
Pd Janus dichalcogenides
Phonon dispersion
Biaxial compressive and tensile strains
Dynamical and mechanical stabilities
Dielectric function
Elastic constants

ABSTRACT

In this work, the effects of compressive and tensile biaxial strain, applied to monolayered 1T Pd Janus PdSSe, PdSTe, and PdSeTe structures are investigated. For tensile strengths larger than 4%, the valence band maxima no longer occur at the high symmetry Γ point; this phenomenon is accompanied by the emergence of a quasi-direct bandgap, where Dirac-like cones develop for large enough strain. A semiconductor-semimetal phase transition takes place for compressive strain strengths of −8%, −4%, and −2% in PdSSe, PdSTe, and PdSeTe respectively. Phonon dispersion calculations show that the Janus structures, subject to tensile strains, are dynamically stable; yet under compressive strains, they are only stable for values not exceeding −6% in PdSSe, −4% in PdSTe, and −2% in PdSeTe. All structures are mechanically stable except for PdSTe under a 14% tensile strain, registering negative in-plane stiffness constants of −9.36 and −7.62 N/m along the x and y directions respectively. Optical absorption/emission within the infrared region is possible when the materials are exclusively subject to tensile strain. Once the Pd Janus structures are synthesized, the results presented here can serve as a guide for the fabrication of optoelectronic devices of optimal performance.

1. Introduction

Two Dimensional (2D) structures were considered thermodynamically unstable [1] till 2004 when the first 2D material, graphene, was isolated from three dimensional (3D) graphite by Novoselov and Geim [2]. Since then, extensive theoretical and experimental studies have been conducted to study its properties that are different from those of graphite: It is a zero bandgap semiconductor, whose conduction and valence bands meet at the Dirac point [3]; it is the thinnest transparent material that absorbs about 2.3% of the incident light, is a hundred times stronger than steel [4], and possesses high electron mobility (~15,000 $cm^2\ V^{-1}\ s^{-1}$) at room temperature [3].

The absence of the finite bandgap has hindered the efficiency of graphene in electronic device applications. Although such a gap can be opened by subjecting a bilayer graphene sheet to an electric field [5], it was important to search for other materials that naturally have this feature. This opened the doors to a myriad of possibilities to extract single layered sheets (2D) from 3D material bulks, leading to interesting properties and applications.

One of those intriguing cases is 2D Transition Metal Dichalcogenides (TMDs) described by a general formula MX_2, M being a layer of a transition metal type sandwiched between the top and bottom layers of a chalcogen X = [S, Se, Te]. These structures have received a lot of attention due to their semiconductor nature and sizable bandgaps ranging between 1 and 2 eV, thus making them relevant in technological applications including field-effect transistors, energy storage devices, and catalysis [6].

The first structures to be studied were group VIB transition metals, namely M = Mo and W [7–9]. From a technological point of view, nanoscale transistors made from MoS_2/$MoSe_2$ monolayers have been already fabricated [10,11]. More applications of 2D MoX_2 and WX_2 involve, but not restricted to, high-capacity information technologies, flexible micro-photonic devices, thermoelectric materials, and nano-electronic devices [12–15]. Also, monolayer TMDs with groups IVB and VB transition metals (such as Ti, Zr, Hf, V, Nb, Ta, and Cr) have been investigated [16–19,20].

Recently the study of 2D layered Janus structures, named after the two-faced God of choices in Roman mythology, have flared up. These have a chemical formula MXY and are constructed by replacing one of the layers of species X in MX_2 with another species Y belonging to the same set, thus obtaining two different layers facing the middle M layer. Experimentally, single layer Janus MoSSe has been synthesized [21,22].

---

* Corresponding author.
E-mail address: eamoujaes@unir.br (Elie.A. Moujaes).

https://doi.org/10.1016/j.mtcomm.2021.102735
Received 31 May 2021; Received in revised form 20 August 2021; Accepted 20 August 2021
Available online 28 August 2021

On a theoretical level, a lot has been done regarding the electronic properties and stability of various Janus MXY TMD monolayers with M = Ti, Hf, Zr, V, Nb, Ta, Cr, Mo and W [23]. [24] have studied the phonon transport in MoSSe. Electronic, elastic and piezoelectric properties of Janus MoSTe were considered in [25]. More interestingly, researchers have even started looking at MoSTe nanotubes [26].

Researchers have equally concentrated on studying WXY monolayers: [27] have examined WSSe as a feasible photocatalyst for water splitting, and [28] have inspected its Raman spectra. The thermoelectric performance of WSTe and WSSe was studied in [29]. WSeTe Janus monolayers were also the focus of a recent research article [30]. On the contrary, only two or three research papers are dedicated to the study of the PdXY dichalcogenide monolayers, namely PdSSe, PdSTe and PdSeTe [31–33].

The modulation of a bandgap is a crucial property that allows the effective utilization of 2D TMDs in electronic and optoelectronic devices. Throughout the years, many strategies such as doping [34], strain engineering, and piling up more layers (thus changing the thickness of the material) [35] have been employed to tune the bandgaps of monolayers of $PdSe_2$, $MoSe_2$ as well as monolayers of Pt dichalcogenides. In particular, the application of strain can, other than varying the bandgap, change the mobility and the effective mass of the electrons. Changes in the vibrational modes of 2D systems, due to the application of strain, have also been described in [36].

When 2D MoS_2 is subjected to a 0.5% compressive strain [37,38], its direct bandgap changed into an indirect one. Furthermore, a semiconductor-metal transition, under a 15% compressive and 6% tensile strains, were noticed in MoS_2 [39,40]. Strain has also been considered in monolayers of WS_2, WSe_2 and WTe_2, with [41] and without [42] the inclusion of the spin-orbit coupling (SOC). Biaxial strain, in particular, was efficient in producing higher strain-induced band tunability than uniaxial strain; a biaxial strain gauge factor 2.3 times the uniaxial strain one was reported in Mos_2 monolayers [43]. Furthermore, it was realized that, in transition metal dichalcogenide monolayers, biaxial strain was useful in regulating the lattice thermal conductivities [44].

As far as the Janus structures are concerned, the effect of strain has been investigated for the more popular MoSSe [45,46] and WSSe structures [47,48]. Additionally, strained PtSSe [49] and ZrSSe [50] were also explored. However, since no work has addressed strain in PdSSe, PdSTe and PdSeTe monolayers, this manuscript will target the effect of both compressive and tensile strain in Janus Pd dichalcogenides. More especifically, we will focus on biaxial strain since, as was mentioned above, it seems to have a more pronounced effect on the materials' properties than uniaxial strain.

The rest of the paper is structured as follows: In section 2, the computational details of the various calculations involved are presented. The electronic structure and partial density of states (PDOS) calculations for different tensile and compressive biaxial strain values are discussed in section 3. Section 4 further examines the phonon dispersion and the dynamical stabilities of the systems in question. Section 5 is reserved for the study of mechanical stability, involving the calculation of the elastic constants. The imaginary part of the dielectric function, needed to investigate the optical absorption and/or emission of the systems, is found in section 6. Conclusions and final considerations follow in section 7.

2. Computational details

The electronic calculations were performed using the plane wave-based Quantum Espresso (QE) package [51]. To enable direct comparison with the unstrained systems already published in [31], the interaction between the valence electrons and the ion cores are treated using the norm-conserving (NC) Troullier-Martins pseudopotential [52]. The exchange-correlation functional is expressed within the Perdew-Burke-Ernzerhof (PBE) parametrization [53] in the Generalized Gradient approximation (GGA). To model the weak Van der Waals (VdW) interactions present in the monolayers, long-range electron correlations are considered within Grimme's semi-empirical [54] method. Dense $24 \times 24 \times 1$ $\mathbf{k}$ grids and a plane wave energy cutoff of 75 Ry are used to ensure the convergence of the electronic calculations. All structures, under different strain strengths, are allowed to relax until the force on each atom is less than 5×10^{-4} Ry/au. Along the direction perpendicular to the plane of the structures, a vacuum distance of 18 Å is added to impede the interaction of the 2D materials with their periodic images. The spin-orbit coupling is not considered in this study.

The phonon dispersion spectra are obtained via the frozen phonon approximation implemented in the PHONOPY code [55], where convergent 2^{nd} order interatomic force constants are calculated using $5 \times 5 \times 1$ supercells and $80 \times 80 \times 1$ $\mathbf{q}$-point meshes. The linear optical properties within the random phase approximation (RPA) [56–58] of the strained systems are investigated through the epsilon.x toolset in QE, by considering the imaginary part of the diagonal components of the dielectric tensor as a function of the frequency ω.

3. Results and discussion

3.1. Electronic bands and partial density of states (PDOS)

Monolayered 1T Janus PdXY structures are three atomic layer thick materials, whose Pd layers are sandwiched between X and Y ($X \neq Y$) layers. In principle, they can be constructed from their pristine 1T PdX_2 analogs by replacing the top (or bottom) X atom with a Y atom (Fig. 1 (a)). Usually X,Y = [S,Se,Te] giving rise to three possible combinations, namely PdSSe, PdSTe, and PdSeTe. All structures have a hexagonal symmetry of the space group P3m1 (Fig. 1(b)). Previous calculations [31] gave optimized lattice parameters of 3.59 Å, 3.73 Å, and 3.81 Å for PdSSe, PdSTe, and PdSeTe respectively. Without SOC, the structures are predicted to be semiconductors with indirect bandgaps of 0.94 eV for PdSSe, 0.34 eV for PdSTe, and 0.33 eV for PdSeTe; these values are in good agreement with other reported theoretical results such as Ref. [59].

The magnitude of biaxial strain (ε) is defined as $(a\text{-}a_{eq}) \times 100/a_{eq}$, where a_{eq} and a depict the unstrained and strained equilibrium lattice parameters respectively. The unstrained materials are stretched up to a maximum strength of 14% and compressed to −8% with an incremental increase of 2%. The new lattice parameters a, corresponding to the different kinds of strain, are found in Table 1. Figs. 2, 3, and 4 display the electronic band structures of the strained Janus structures. For tensile strains, the bandgap increases reaching a maximum of around 2% in PdSSe, and then starts to decrease for higher values. For strains larger than or equal to 4%, the valence band maxima (VBM) (corresponding to the highest value of the valence band energies along the whole Γ-K-M-Γ path) shifts its position from the Γ point to another point along the Γ-K path. Also, another point along the M-Γ path erupts having energy close to, but accurately a bit larger than the first point, insinuating the birth of a quasi-direct bandgap. There is a clear decline in the values of the bandgaps that reach a minimum of 0.31 eV for a 14% strain. On the other hand, the conduction band minima (CBM) (corresponding to the minimum value of the conduction band energies along Γ-K-M-Γ), which was along the M-Γ for the unstrained system, now resides at a point along the Γ-K path. At a −8% compressive strain, the structure has already turned into a semimetal.

A similar pattern is observed for PdSTe. The indirect bandgaps increase up to an applied strain of 4%, above which the VBM also switch to a point along the Γ-K direction. The difference in energy between the indirect and quasi-direct bandgaps is smallest (~ 20 meV) for $\varepsilon = 14\%$. Likewise, the CBM whose position was around the K point moves to a point along the M-Γ path for $6\% \leq \varepsilon \leq 14\%$. The semi-conductor-semimetallic transition takes place for compressive strains larger than or equal to −4%.

At large strain values, it becomes clear that all the quasi-direct bandgaps are accompanied by shifted Dirac-like cones, that occur at

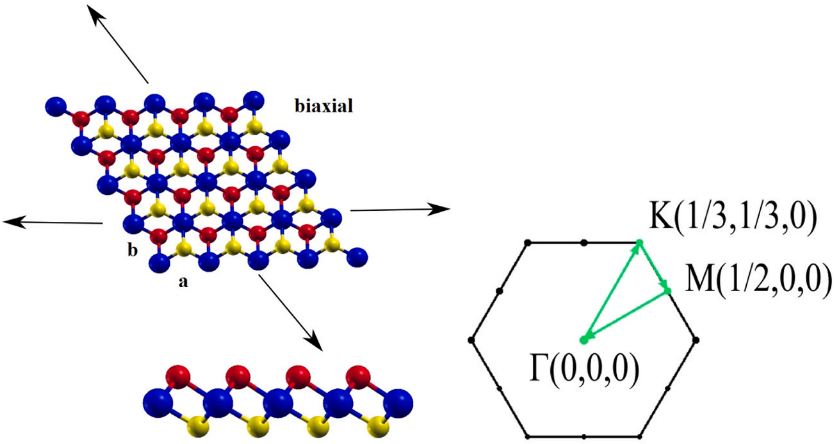

(a) (b)

Fig. 1. (Color Online) (a) Top and side views of a (4 × 4) supercell of the unstrained 2D 1T PdXY structures, showing the biaxial strain's directions (along **a** and **b**). Blue spheres are Pd atoms, whereas red and yellow spheres refer to the X and Y elements respectively. (b) The Brillouin zone (BZ) of the unstrained PdXY structures showing the Γ-K-M-Γ path.

Table 1

The lattice parameters (*a*), the indirect (E_g^I) and quasi-direct (E_g^D)) bandgap values for the unstrained and biaxially strained (both tensile and compressive) cases. For E_g^I, the "—" symbol means that the structure is gapless, while for E_g^D it means that the structure does not possess a quasi-direct bandgap.

System		**Compressive**				**Unstrained**	**Tensile**						
		-8%	-6%	-4%	-2%	0%	2%	4%	6%	8%	10%	12%	14%
PdSSe	a (Å)	3.30	3.37	3.44	3.51	3.59	3.67	3.73	3.80	3.87	3.95	4.02	4.09
	E_g^I (eV)	0.00	0.19	0.48	0.74	0.94	1.02	0.98	0.84	0.69	0.55	0.44	0.31
	E_g^D (eV)	—	—	—	—	—	—	1.01	0.87	0.72	0.70	0.47	0.33
PdSTe	a (Å)	3.43	3.51	3.58	3.66	3.73	3.80	3.88	3.96	4.03	4.10	4.17	4.25
	E_g^I (eV)	—	—	—	0.11	0.33	0.54	0.60	0.52	0.39	0.27	0.17	0.16
	E_g^D (eV)	—	—	—	—	—	—	0.64	0.55	0.42	0.29	0.19	0.18
PdSeTe	a (Å)	3.50	3.58	3.65	3.73	3.81	3.88	3.96	4.03	4.11	4.19	4.26	4.34
	E_g^I (eV)	—	—	—	0.06	0.34	0.52	0.59	0.44	0.31	0.18	0.08	0.02
	E_g^D (eV)	—	—	—	—	—	—	0.59	0.46	0.34	0.20	0.11	0.09

nonsymmetrical points in the BZ. As is well known, Dirac cones (gapless) were first identified in graphene [60]. In strained graphene, these features remain but move to different positions [61]. Unlike this material, the Dirac cones in the 1T Pd Janus materials are not gapless; they also do not show up for the unstrained cases.

In PdSeTe, the semiconductor-semimetallic transition outbreaks at compressive strains as small as -2%. For tensile strengths, the difference in energy between the indirect and quasi-direct bandgaps is largest ($\sim$ 70 meV) when $\varepsilon = 14\%$. As was observed in both 1 T PdSSe and PdSTe materials, the drop in the indirect bandgap value is faster for compressive strains. Note that applying a compressive strain does not favor the formation of quasi-direct band gaps; its net effect is a rapid reduction of the indirect bandgap. Detailed values of the indirect (E_g^I) and quasi-direct (E_g^D) bandgaps for the three Janus systems can be found in Table 1. The variation of E_g^I with respect to ε is displayed in Fig. 5.

The quasi-direct bandgap phenomenon has been recently observed in 2D hexagonal unstrained SnTe structures [62], and in some silicon allotropes [63]. It is also quite similar to what characterizes 2D monolayers of WS_2 [41,64], WSe_2, and WTe_2 [41]. Furthermore, the increase-decrease pattern of the bandgap is not new, and has previously appeared in NiS_2 and PdS_2 under tensile strain [65]. A comparable comportment also occurs for 2D ZrS_2 monolayers; the bandgap increases for a tensile strain, reaching a maximum value for $\varepsilon = 6\%$ and decreases in the case of compressive strains, until the material becomes metallic for compressive strains larger than -8% (Fig. 6).

Fig. 7.

Fig. 8.

In regard to Janus materials reported in the literature, the indirect bandgap in 1 T SnSSe monolayers increases for a tensile strain, attaining a value of $\sim$1.12 eV for $\varepsilon = 6\%$ and decreases to $\sim$0.37 eV for a compressive strain of $\varepsilon = -6\%$ [66]. Compared to the 1 T PdSSe, the bandgaps in SnSSe are larger with no signs of a bursting quasi-direct bandgap. In Janus Mo and W TMD monolayers, the bandgap decreases for tensile strain; it then increases and decreases again for a compressive strain and changes from being direct (tensile cases) to indirect (compressive cases) [67]. Figs. 6, 7, and 8 illustrate the electronic partial density of states (PDOS) in PdSSe, PdSTe, and PdSeTe for $\varepsilon = -2\%$ and 8%. As expected, the results conform with the electronic bands: compared to the unstrained cases, the bandgaps for all systems are reduced. The semimetallic nature of PdSeTe is also apparent under a -2% strain, giving a non-zero density of states in the vicinity of E_F. For -1.6 eV $\leq$ E-$E_F \leq$ 0 eV, the contributions of the S and Se to the valence bands, close to E_F, are higher than those of the Pd atoms, which contribute more to the conduction bands; still, such contribution is smaller than that of the chalcogenides. Before delving into the optical properties of the strained materials at hand, a discussion of their dynamical and mechanical stabilities is firstly in order (Fig. 9).

4. Phonon dispersion and dynamical stability

Since the Janus PdXY structures have three atoms per unit cell, this results in a total of nine dispersion curves, the first three of which correspond to acoustic (A) modes, and the rest refers to optical (O)

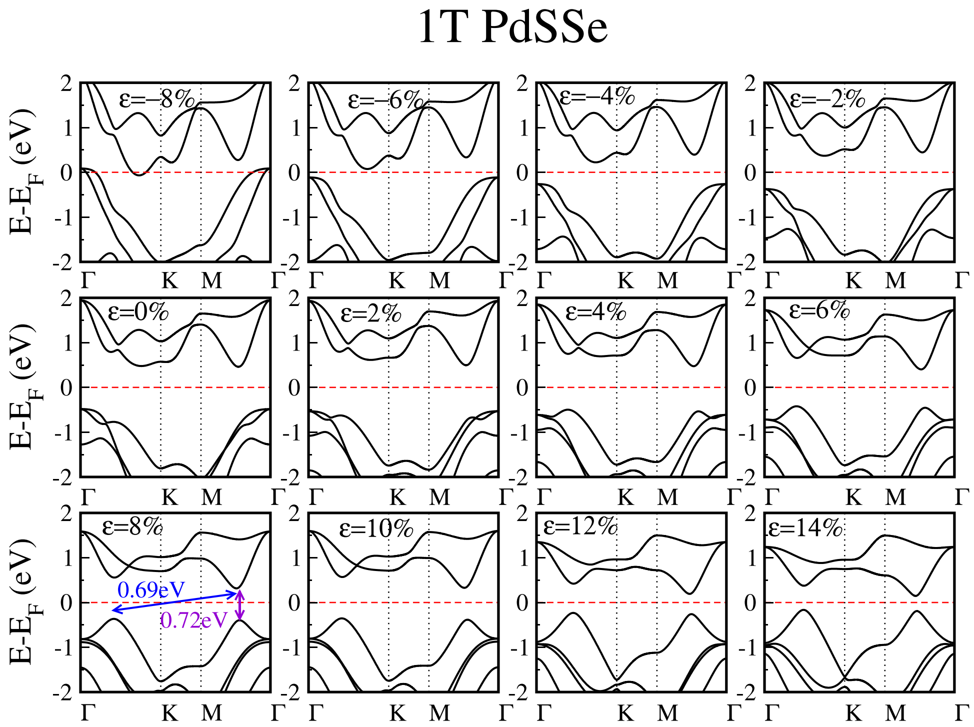

Fig. 2. (Color Online) Electronic band structures of 1T PdSSe for strains between −8% and 14% where for the semiconductors, E_F is placed at the middle of the gaps. For $\varepsilon \geq 4\%$, the VBM shifts from the Γ point to another point along the Γ-K path (indirect bandgap shown in blue). The quasi-direct bandgap, only illustrated for $\varepsilon = 8\%$, is represented by the double headed violet arrow.

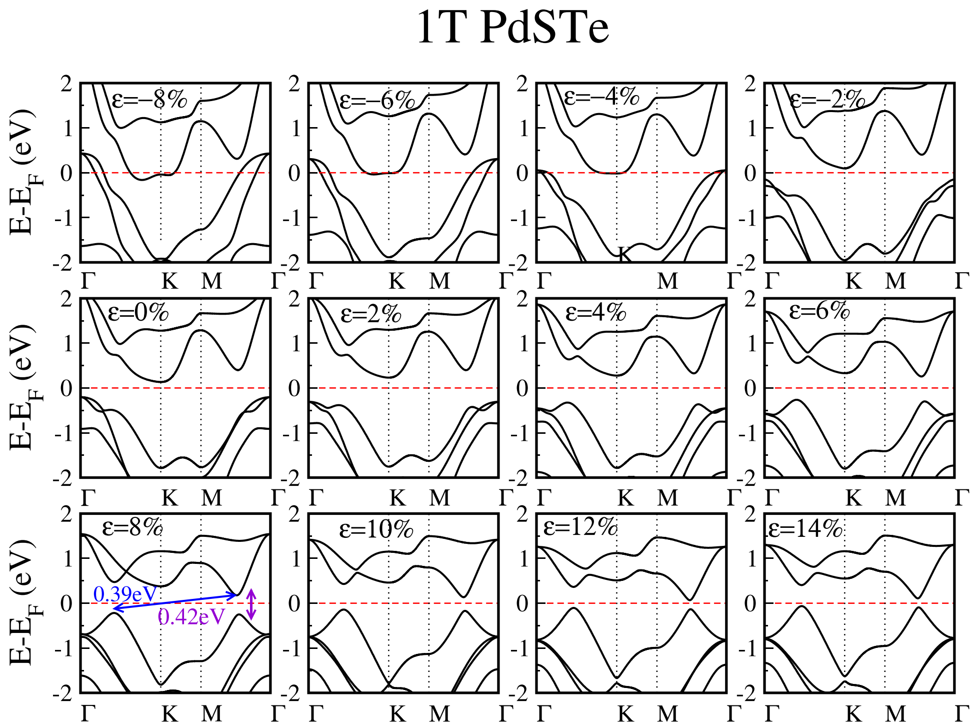

Fig. 3. (Color Online) Electronic band structures of 1T PdSTe for the same strain strengths applied to PdSSe. The VBM moves to a point along the Γ-K path for $\varepsilon \geq 4\%$. A quasi-direct bandgap, shown in violet for the 8% strain case, erupts along the M-Γ path. The indirect bandgap is represented by the tilted double-headed blue arrow.

modes. All modes can be further classified as either longitudinal (L), transverse (T), or flexural (Z). Both longitudinal and transverse modes are in-plane modes, while the flexural mode represents an out-of-plane vibration of the atoms. All nine modes are both Infrared (IR) and Raman (R) active [51,55] (Fig. 10).

Fig. 11.

Figs. 9, 10, and 11 display the phonon dispersion spectra of 1T PdSSe, PdSTe, and PdSeTe for various tensile and compressive strain

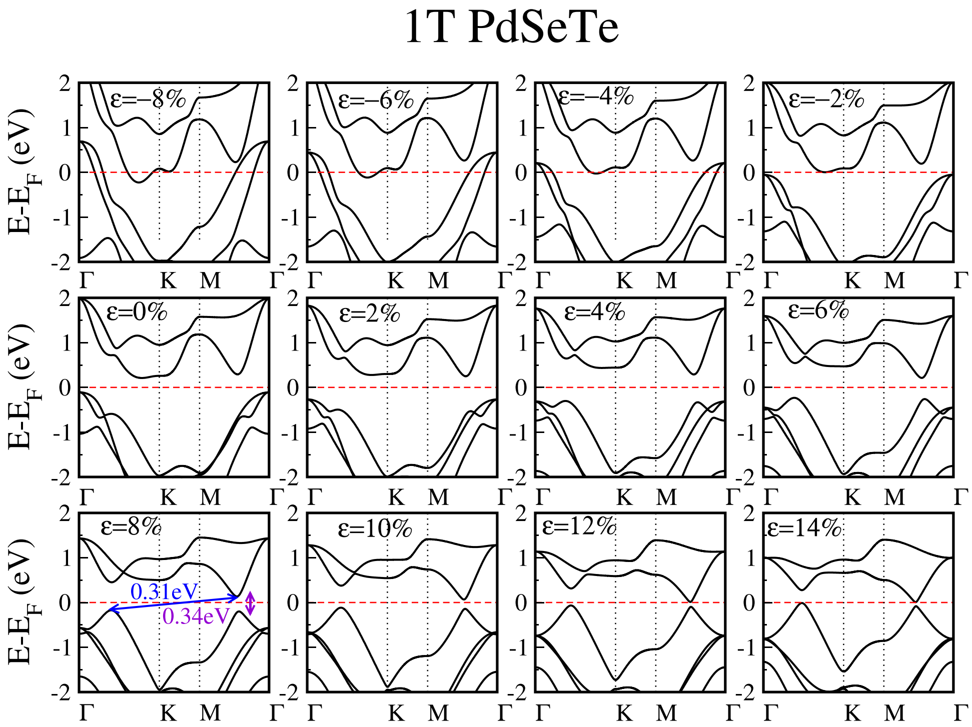

Fig. 4. (Color Online) Same as Figs. 2 and 3 but for 1T PdSeTe. For $\varepsilon = 8\%$, the energy difference between the indirect and the quasi-direct bandgaps is around 30 meV.

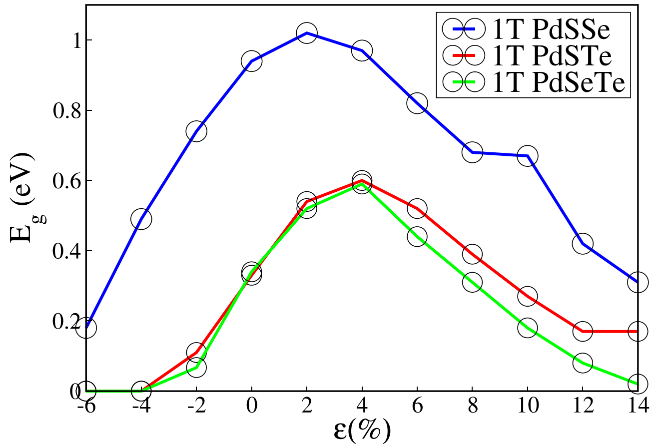

Fig. 5. (Color Online) The change of the indirect bandgap energy as a function of compressive and tensile strain strengths.

strengths. For comparison purposes, the dispersions of the unstrained materials are also shown. All structures under tensile strain are dynamically stable. However, very small negative (imaginary) frequencies, for points near Γ, are observed possibly due to numerical inaccuracies in diagonalizing the dynamical matrix. Under compressive strain, PdSSe, PdSTe, and PdSeTe are stable up to values of -6%, -4%, and -2% respectively. For larger strains, the phonon spectra exhibit large spaghetti-like negative frequencies throughout the whole BZ, indicating dynamical instability.

To understand the asymmetry between tensile and compressive strains, Fig. 12 shows how the z-component of the Pd atom changes as the tensile/compressive strain is increased. Compared to the unstrained case, the variation in the perpendicular positions of the Pd atoms in PdSSe reaches 23.18% for a -8% strain whereas it only reaches 14.86% for a $+8\%$ compressive strain. The changes are more pronounced in PdSTe, where a -8% compressive strain causes a change of 38.17%, compared to a 22.68% change for a $+8\%$ tensile strain. In PdSeTe, a strain of just -2% is capable of a 64% change in Pd's atomic position; strikingly for a $+2\%$ strain, the change does not exceed 21.38%.

To further monitor what is actually happening to the 1 T structures upon the application of strain, Fig. 13 portrays the side view of PdSSe, PdSTe and PdSeTe under several compressive and tensile strain strengths. At some point, and as the compressive strain increases, the Pd-S, Pd-Se, and Pd-Te bonds seem to increase in length with no drastic changes (no bond breaking) to the trigonal 1 T environment. Although The PdSSe, PdSTe and PdSeTe structures are not dynamically stable for $\varepsilon \geq -8\%$, -6% and -4% respectively, they can still be mechanically stable (as can be confirmed from Table 2 for $\varepsilon = -4$ and -8%). Thus these cases, in particular, can represent metastable states that cannot be experimentally realized.

Under tensile strain, the structures preserve their 1 T trigonal environment up to $\varepsilon = 12\%$. For larger values of strain, it is evident that the bonds start to loosen up and the trigonal 1 T feature is completely lost when $\varepsilon \geq 20\%$. This is in agreement with the phonon dispersions and elastic constant results (refer to Table 2), which show that up to $\varepsilon = 12\%$, the structures are both mechanically and dynamically stable.

As one scans the systems over the various tensile strain strengths, it is noticed that the three lowest and three highest optical modes become closer to each other, reducing the optical-optical bandgap throughout the whole BZ path. These modes get mixed for $\varepsilon = 12\%$ in PdSSe and for $\varepsilon = 10\%$ in PdSTe. Per contra, it is the acoustical-optical bandgap that suffers a reduction along the K-M path in PdSeTe; for $\varepsilon \geq 10\%$, both the acoustical and low-lying optical modes get intermingled, an aspect not observed when compressive strain is applied. This implies that a large tensile strain in PdSeTe could increase the rate of the phonon scattering processes, leading to a decrease in the phonon lifetime and consequently a decline in the lattice thermal conductivity. Such a system could thus be a crucial element in the production of potent thermoelectric devices.

5. Mechanical stability of the strained structures

Strain changes the lattice vectors of the unit cell and is expected to

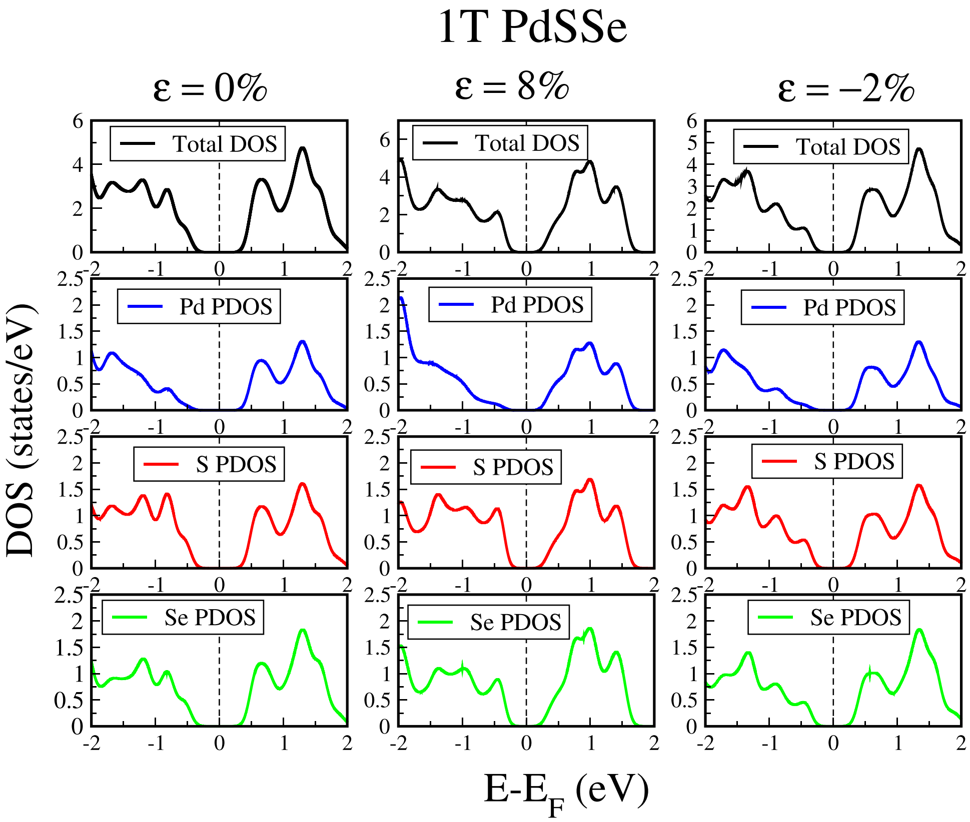

Fig. 6. (Color Online) The total and Partial density of states (PDOS) of the PdSSe structure subject to compressive and tensile strengths $\varepsilon = -2\%$ and 8%. The unstrained case has been included to facilitate comparison.

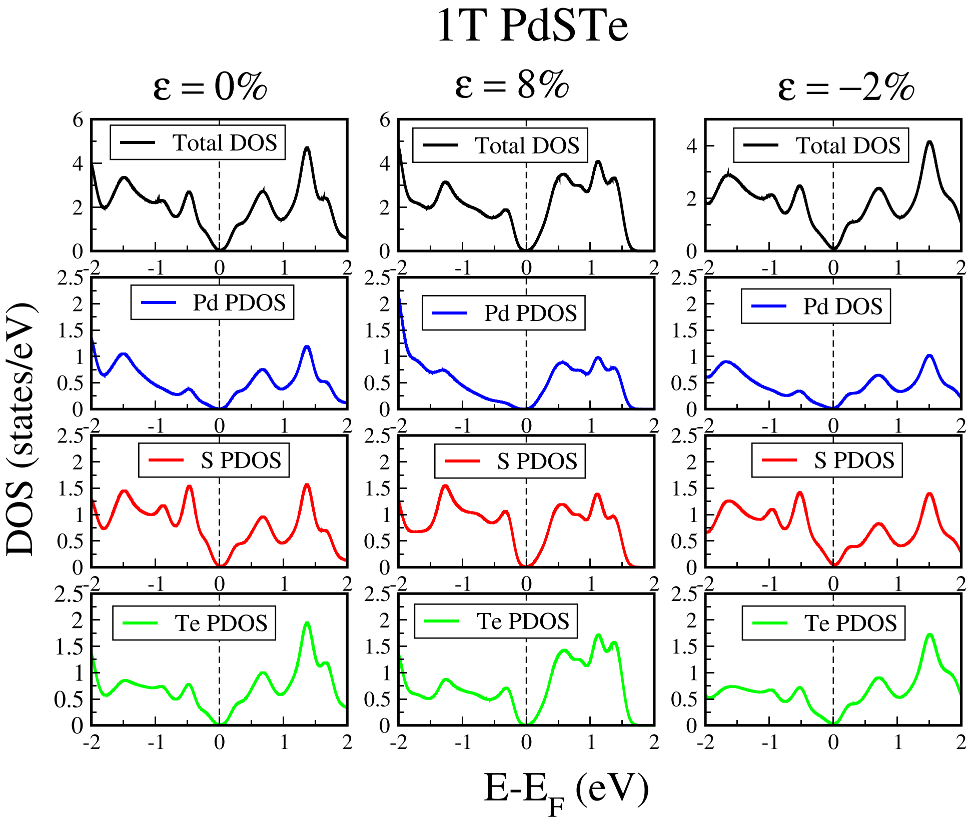

Fig. 7. (Color Online) Same as Fig. 6 but for the PdSTe system.

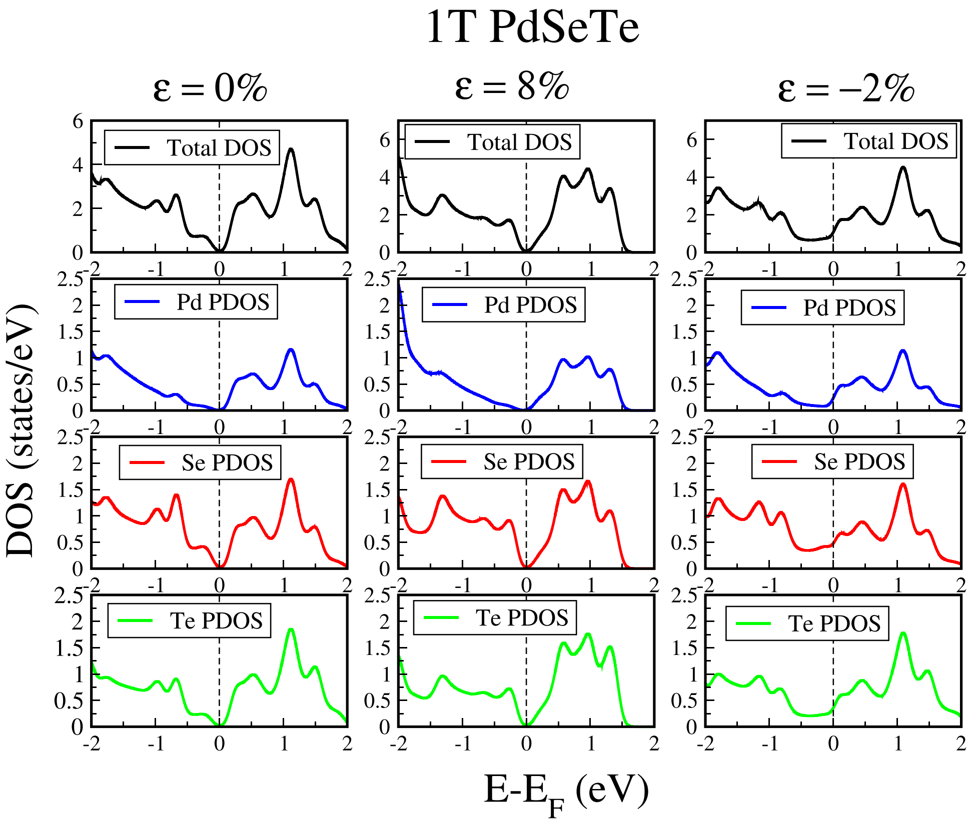

Fig. 8. (Color Online) Same as Figs. 6 and 7 but for the PdSeTe system.

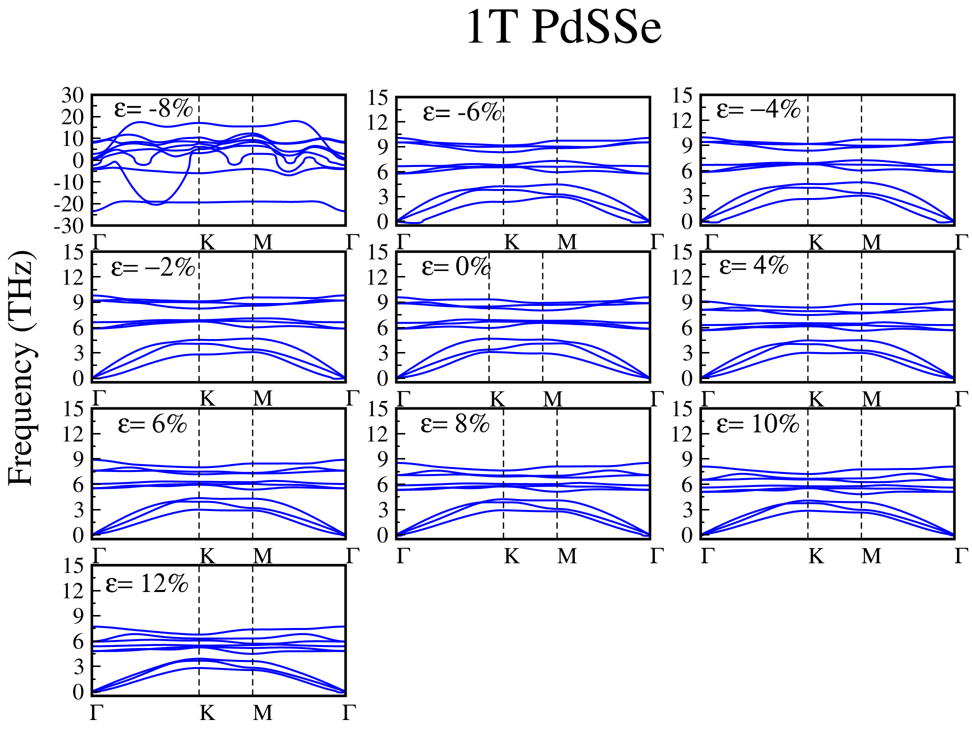

Fig. 9. (Color Online) Dispersion spectra for 1T PdSSe under tensile and compressive strain. Large spaghetti-like negative modes, signaling instability, are evident for compressive strains larger than or equal to −8%.

have an impact on the elasticity of the material. The in-plane elastic constants C_{2D} for the 1 T PdSSe, PdSTe, and PdSeTe materials have been evaluated for each strain value. Generally, for a 2D material of hexagonal symmetry, the number of independent in-plane elastic constants is reduced to two, namely $C_{11} = C_{22}$, along the x and y directions, and the so-called shear modulus (C_{66}), from which one defines C_{12}

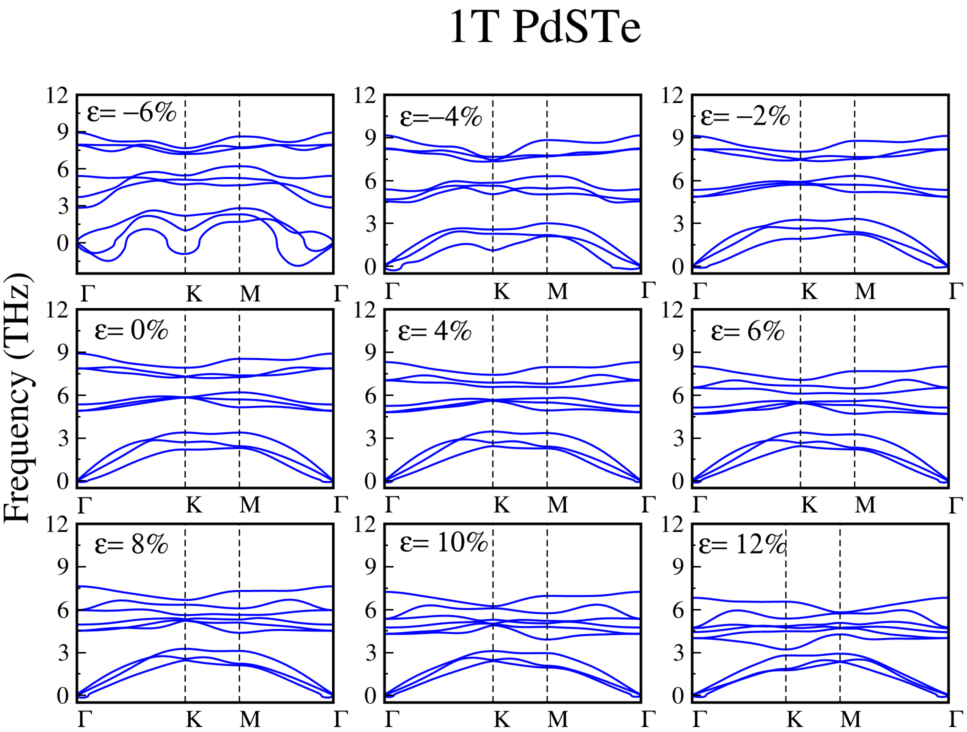

Fig. 10. (Color Online) Same as Fig. 9 but for 1T PdSTe. Structures, under compressive strains larger than or equal to −6%, are dynamically unstable.

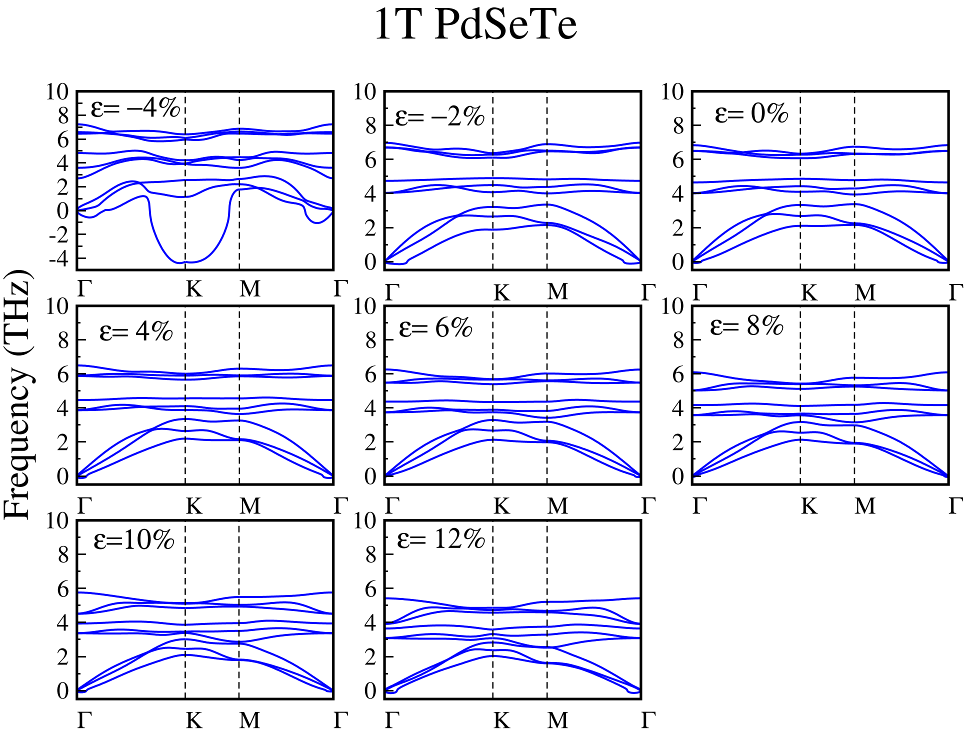

Fig. 11. (Color Online) Same as Figs. 9 and 10 but for 1T PdSeTe structures. Dynamical instability is observed for compressive strains larger than or equal to −4%.

= C_{11}-2C_{66}. Upon the application of a tiny distortion in the neighborhood of each of the relaxed strained structures, the new planar lattice vectors ($\vec{a}'$ and $\vec{b}'$) that incorporate the C_{11}, C_{22} and C_{66} calculations become:

$$\vec{a}' = (1+\delta_1)a \quad \hat{\boldsymbol{x}} + a\delta_6/2 \quad \hat{\boldsymbol{y}}\, \vec{b}' = (-\frac{1}{4}(2+2\delta_1-\sqrt{3}\,\delta_6/2))a \quad \hat{\boldsymbol{x}} + (\frac{1}{4}(2\sqrt{3}+2\delta_2\sqrt{3}-\delta_6))a \quad \hat{\boldsymbol{y}},$$

where δ_1, δ_2, and δ_6 are the infinitesimal distortions taken between −0.015 and 0.015, a is the lattice parameter for the strained material,

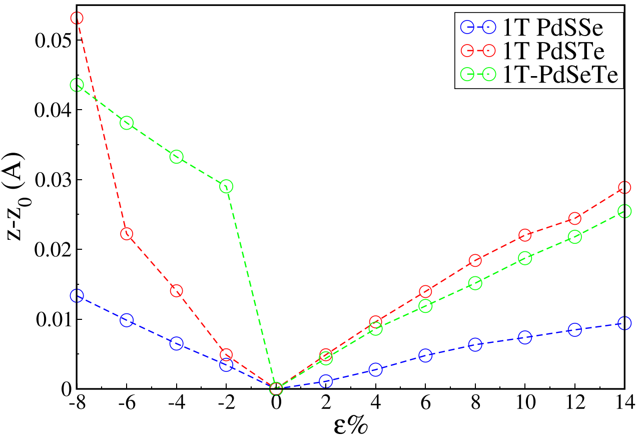

Fig. 12. (Color Online) The change of the positions of the Pd atoms along the direction perpendicular to the structures (z), relative to the their positions for the unstrained case (z_0). Starting from PdSSe, and moving towards PdSeTe, it can be seen that such a change is more noticeable for the compressive strain.

and $\hat{x}$ and $\hat{y}$ are unit vectors along the x and y directions respectively. C_{11} is evaluated by setting $\delta_2 = \delta_6 = 0$, and C_{66} corresponds to the solution where both δ_1 and δ_2 are zeros. The energy E versus strain is then fit to quadratic equations of the form:

$$E_\delta = a_1 + a_2\delta + a_3\delta^2,$$

a_1, a_2, and a_3 being fitting parameters and $\delta = \{\delta_1, \delta_2, \delta_6\}$. By defining $C_{\alpha\alpha} = \frac{1}{A_0}\frac{dE^2}{d\delta^2}\Big|_{\delta=0}$, one gets that $C_{\alpha\alpha} = 2a_3/A_0$ for $\alpha = 1,2,6$; A_0 is the area of the corresponding hexagonal unit cell given by $\sqrt{3}a^2/2$. The 2D Young's modulus, along the $a \equiv x$ and y directions, can be determined via the expressions [68]:

$$C_{2D}^{a} = \frac{C_{11}C_{22} - C_{12}^2}{C_{22}}$$

$$C_{2D}^{y} = \frac{C_{11}C_{22} - C_{12}^2}{C_{11}}.$$

The elastic constants, found in Table 2, show that $C_{11} \simeq C_{22}$ with deviations not exceeding 3.7%, mainly due to numerical noise in the calculations of E_δ. According to the Born criteria [68], all elastic constants are positive indicating that the Janus structures are mechanically stable. The only exception is PdSTe under $\varepsilon = 14\%$, where both C_{66} and C_{2D} are negative signifying instability. Furthermore, structures under compressive strains of -4% and -8% are mechanically stable, despite their dynamical instability. As one moves from compressive towards tensile strains, C_{2D} decreases. This is not surprising since, as strain grows, it tends to weaken the interatomic forces.

6. Optical properties

Within the rigid phase approximation, the tensor components of the complex dielectric function $\varepsilon_2(\omega)$, as a function of the frequency ω, can be defined as [69]:

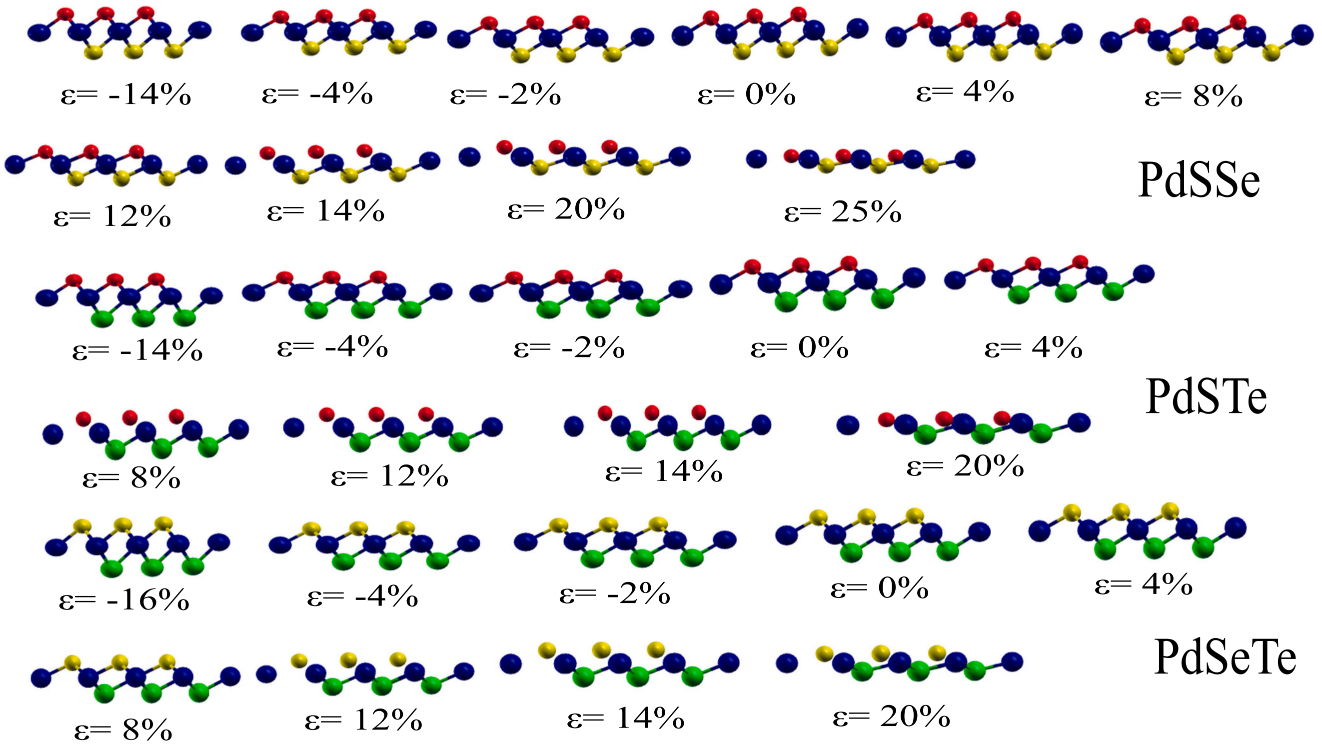

Fig. 13. (Color Online) Side view of 1 T PdSSe, PdSTe and PdSeTe structures under various compressive and tensile strains. Blue spheres represent Pd atoms; red, yellow and green balls correspond to S, Se and Te atoms respectively. For tensile strains as large as 20%, the structures have already lost their 1 T trigonal feature. PdSSe and PdSTe Structures with $\varepsilon = -8\%$, and PdSeTe under a -4% strain are mechanically stable but dynamically unstable, indicating that they cannot be experimentally synthesized.

Table 2
Elastic constants and the 2D Young’s modulus along the x and y directions, in units of N/m, for the Janus 1Tstrained PdSSe, PdSTe and PdSeTe systems.

	Strain (%)	C_{11}	C_{22}	C_{12}	C_{66}	C^{x}_{2D}	C^{y}_{2D}
PdSSe	-8%	72.65	72.71	21.42	25.63	66.34	66.39
	-4%	78.66	78.74	24.75	26.97	70.88	70.95
	-2%	75.61	75.61	23.67	25.97	68.21	68.21
	0%	68.03	70.59	20.06	24.62	62.33	64.68
	2%	64.80	64.85	18.63	23.09	59.45	59.49
	4%	57.89	57.88	15.40	21.24	53.79	53.78
	6%	50.88	50.86	11.76	19.56	48.16	48.14
	8%	44.00	43.99	8.57	17.71	42.33	43.32
	10%	36.87	36.76	5.33	15.74	36.10	35.98
	12%	29.58	29.32	2.23	13.61	29.41	29.16
	14%	21.55	21.42	-0.89	11.19	21.52	21.38
PdSTe	-8%	35.65	37.06	11.88	11.88	31.84	33.10
	-4%	56.98	56.55	16.81	20.09	51.98	51.60
	-2%	54.70	54.64	16.57	19.07	49.67	49.62
	0	53.27	53.15	16.45	18.41	48.17	48.07
	2%	50.84	50.67	15.87	17.48	45.86	45.72
	4%	47.28	47.26	14.68	16.29	42.72	42.70
	6%	41.54	41.81	12.88	14.33	37.57	37.82
	8%	34.64	35.06	10.85	11.90	31.29	31.67
	10%	25.99	26.50	8.37	8.81	23.35	23.80
	12%	15.37	15.44	7.33	4.02	11.88	11.94
	14%	3.01	2.98	5.51	-1.25	-9.36	-7.62
PdSeTe	-8%	50.45	52.18	13.93	18.26	46.73	48.33
	-4%	58.29	58.03	18.30	19.99	52,52	52.28
	-2%	57.73	57.52	18.42	19.66	51.83	51.64
	0	56.00	55.72	17.79	19.11	50.32	50.07
	2%	47.44	47.27	16.59	18.04	47.44	47.27
	4%	47.78	47.55	14.62	16.58	43.28	43.07
	6%	41.72	41.10	11.99	14.86	38.22	37.62
	8%	34.67	34.86	8.99	12.84	32.35	32.53
	10%	26.55	26.91	6.07	10.24	25.18	25.55
	12%	16.95	16.78	3.44	6.75	16.25	16.09
	14%	5.39	5.36	0.68	2.35	5.30	5.27

$$
\begin{aligned}
\varepsilon_{\alpha,\beta}(\omega) &= 1-\frac{4\pi q^2}{VN_k m^2}\sum_{n,k}\frac{df(E_{k,n})}{dE_{k,n}}\\
&\times \frac{\widehat{M}_{\alpha,\beta}}{\omega^2+i\eta\omega}+\ldots+\frac{8\pi q^2}{VN_k m^2}\\
&\times \sum_{n\neq n'}\sum_{k}\frac{\widehat{M}_{\alpha,\beta}}{E_{k,n'}-E_{k,n}}\ldots\\
&\ldots \frac{f(E_{k,n})}{(\omega_{k,n'}-\omega_{k,n})^2+\omega^2+i\Gamma\omega},
\end{aligned}
$$

where V is the volume of the unit cell, and N_k is the number of points sampling the reciprocal BZ. q is the electron’s charge and m is its mass. $E_{n,k}$ and $E_{n',k}$ are the energies of the k^{th} point in the valence band n and conduction band n' respectively. The matrix elements $\widehat{M}_{\alpha,\beta}$ are the result of the evaluation of momentum operators between Bloch states, directly obtained from a plane waves’ DFT calculation in QE. Finally, Γ and η are intersmear and intrasmear Gaussian broadening parameters respectively. Up to an energy of 3.3 eV, the isotropic in-plane components of the imaginary part of ε_2 ($\varepsilon''_{2,xx} \equiv \varepsilon''_{2,yy}$) for some stable strained structures are displayed in Fig. 14. When tensile strains are applied, all major maxima in the absorption spectra move towards the IR region. In PdSSe, the peaks appear at 1.56, 1.14, 0.81, and 0.54 eV for $\varepsilon = 0\%$, 4%, 8%, and 12% respectively. In PdSTe, they occur at 1.26, 0.81, 0.51, and 0.24 eV and are observed at 1.26, 0.75, 0.41, and 0.14 eV in PdSeTe. These redshifts are only noticed for strains larger than or equal to 4%, cases that correspond to the movement of the VBM from the Γ point to points where Dirac-like cones start to form. Furthermore, the shifting of the peaks is not detected under compressive strains, suggesting that the absorption spectra are unaffected. For a PdSeTe structure under $\varepsilon = -2\%$, $\varepsilon''_2(0)$ is non zero, conceivably due to the semimetallic nature of this material.

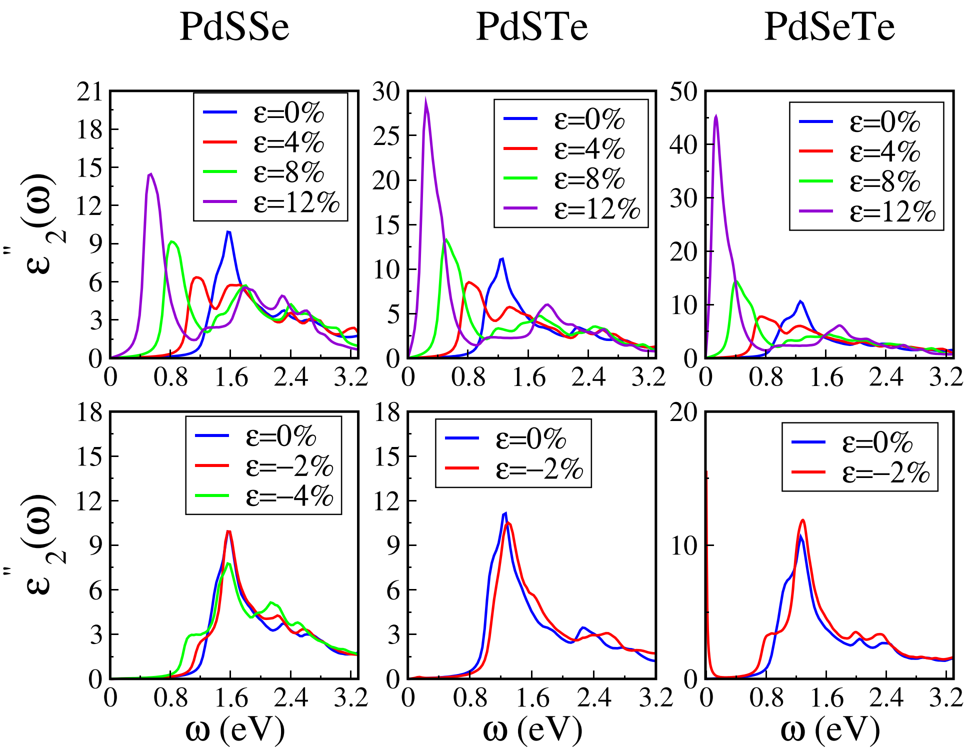

Fig. 14. (Color Online) The in-plane components of the imaginary part of the dielectric function ($\varepsilon''_2(\omega)$) within the IR-visible electromagnetic spectrum for Janus PdSSe, PdSTe, and PdSeTe subject to various tensile and compressive strains. As the tensile strain increases, the absorption/emission maxima approach the IR region. The locations of the maxima are not altered by the application of compressive strains.

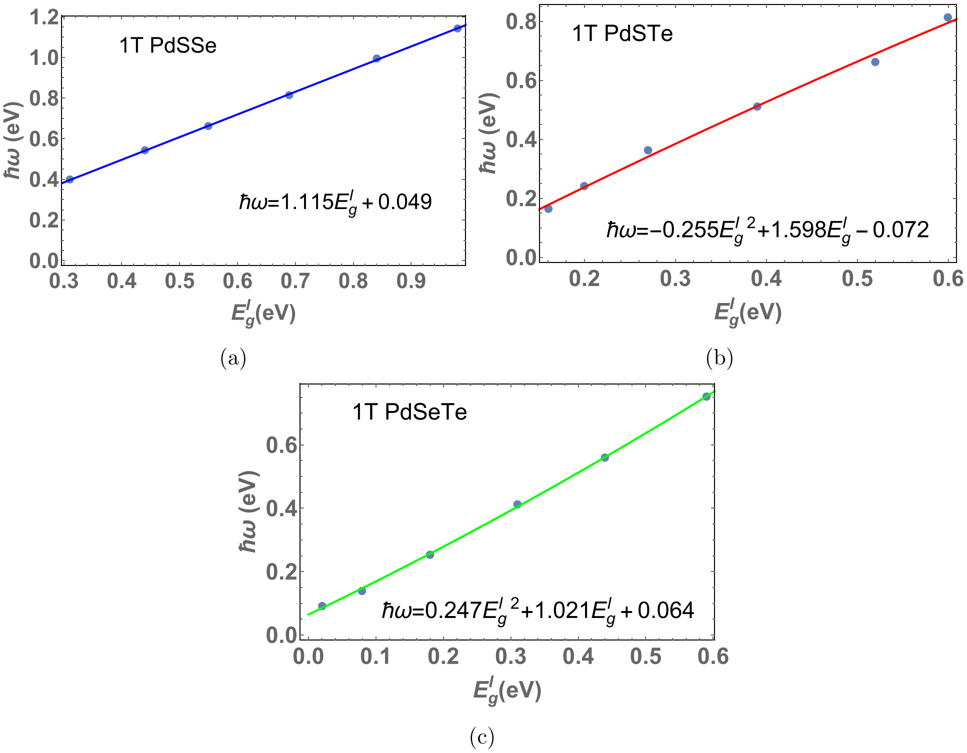

(a) (b) (c)

Fig. 15. (Color Online) The evolution of the energies at the absorption maxima in PdSSe, PdSTe, and PdSeTe as a function of the indirect bandgap, for different strain systems corresponding to $\varepsilon \geq 4\%$. In PdSSe, the points could be fitted to a straight line; in PdSTe and PdSeTe, the best fit is a parabola.

Fig. 15 displays the variation of the energies at which the absorption/emission maxima occur, as a function of the indirect band gaps for $\varepsilon \geq 4\%$. In PdSSe, the points could be fitted to a straight line, whereas for the data related to strained PdSTe and PdSeTe, the best fit is a parabola. The calculations demonstrate that, under a tensile strain of 14%, the maximum absorption in PdSeTe takes place around 0.09 eV, which is close to the "zero" energy; this proposes that, at larger strain values, the system is tending to a semimetallic phase. By extrapolating the values, making use of the parabolic fitting curve, the PdSTe structure is expected to convert into a semimetal when $\varepsilon \sim 15.5\%$; however, at this strain value, the structure has already mechanically destabilized, as can be inferred from the values of the elastic constants in Table 2.

7. Conclusion

In this work, the effect of biaxial tensile and compressive strains on 1 T monolayers of Janus PdSSe, PdSTe, and PdSeTe is probed. Compressive strains tend to reduce the bandgaps in the structures faster than tensile strains of the same strength do. The indirect bandgap reaches a maximum for $\varepsilon = 2\%$ in PdSSe and $\varepsilon = 4\%$ in PdSTe and PdSeTe, decreasing to 0.02 eV for $\varepsilon = 14\%$ in PdSeTe. For $\varepsilon \geq 4\%$, the valence band maxima shift from the Γ point to a point along the Γ-K directions, with the emergence of a quasi-direct bandgap accompanied by Dirac-like cones. This phenomenon is restricted to tensile strain cases and is not seen when compressive strains are applied. Under compressive strains, a semiconductor-semimetal transition takes place for strains larger than −8% in PdSSe, −4% in PdSTe, and −2% in PdSeTe.

Phonon dispersion calculations show that all systems subject to tensile strains are dynamically stable whereas, under compressive strains, 1 T PdSSe, PdSTe, and PdSeTe monolayers are stable up to $\varepsilon = -6\%$, −4% and −2% respectively. Additionally, as the tensile strain increases, the mixing of the three lowest and three highest optical modes occurs for $\varepsilon \geq 12\%$ in PdSSe and ≥10% in PdSTe. In PdSeTe, it is the acoustical and optical modes that get mixed instead. Such reductions in the phonon bandgaps could decrease the phonon lifetime and consequently reduce the lattice thermal conductivity; this, in turn, would lead to higher figures of merit, making the systems perfect candidates for powerful thermoelectric devices.

In an attempt to determine the 2D in-plane Young's modulus, the elastic constants were calculated; as tensile strain increases, the materials become less stiff due to the weakening of the interatomic forces. All strained systems are mechanically stable, except the 1 T PdSTe material under $\varepsilon \geq 14\%$, which possesses negative in-plane elastic constants of −9.36 and −7.62 N/m along the x and y directions respectively.

An investigation of the optical properties have revealed that, as the tensile strain becomes larger than 4%, the absorption/emission peaks occur at smaller frequencies within the IR region, suggesting that the tensile-strained Pd Janus TMDs could be used in optoelectronic devices that function at various IR wavelengths. This phenomenon is not perceived when compressive strains are applied, where the absorption/emission maxima remain at the same positions as those of the unstrained systems.

The results presented in this article are extremely beneficial in tuning the optical properties in Janus Pd dichalcogenides, and pave the way to explore the thermoelectric features of such systems. Furthermore, they can be experimentally verified, once the Pd Janus structure are synthesized.

Declaration of Competing Interest

The authors declare that they have no known competing financial interests or personal relationships that could have appeared to influence the work reported in this paper.

Data Availability

The data that supports this study are available within this article.

Acknowledgments

The simulations in this work were performed at King AbdulAziz University's High Performance Computing Center (Aziz HPCC) (http://hpc.kau.edu.sa).

References

[1] N.D. Mermin, Crystalline order in two dimensions, Phys. Rev. 176 (1) (1968) 250.

[2] K.S. Novoselov, A.K. Geim, S.V. Morozov, D. Jiang, Y. Zhang, S.V. Dubonos, I. V. Grigorieva, A.A. Firsov, Electric field effect in atomically thin carbon films, Science 306 (5696) (2004) 666–669.

[3] A.K. Geim, K.S. Novoselov, The rise of graphene, in: Nanoscience and Technology: A Collection of Reviews from Nature Journals, World Scientific, 2010, pp. 11–19.

[4] F. Liu, P. Ming, J. Li, Ab initio calculation of ideal strength and phonon instability of graphene under tension, Phys. Rev. B 76 (6) (2007), 064120.

[5] E. McCann, Asymmetry gap in the electronic band structure of bilayer graphene, Phys. Rev. B 74 (16) (2006), 161403.

[6] G.R. Bhimanapati, Z. Lin, V. Meunier, Y. Jung, J. Cha, S. Das, D. Xiao, Y. Son, M. S. Strano, V.R. Cooper, et al., Recent advances in two-dimensional materials beyond graphene, ACS Nano 9 (12) (2015) 11509–11539.

[7] Q.H. Wang, K. Kalantar-Zadeh, A. Kis, J.N. Coleman, M.S. Strano, Electronics and optoelectronics of two-dimensional transition metal dichalcogenides, Nat. Nanotechnol. 7 (11) (2012) 699–712.

[8] M. Chhowalla, H.S. Shin, G. Eda, L.-J. Li, K.P. Loh, H. Zhang, The chemistry of two-dimensional layered transition metal dichalcogenide nanosheets, Nat. Chem. 5 (4) (2013) 263–275.

[9] Y. Li, Z. Zhou, S. Zhang, Z. Chen, Mos2 nanoribbons: high stability and unusual electronic and magnetic properties, J. Am. Chem. Soc. 130 (49) (2008) 16739–16744.

[10] H. Liu, M. Si, Y. Deng, A.T. Neal, Y. Du, S. Najmaei, P.M. Ajayan, J. Lou, P.D. Ye, Switching mechanism in single-layer molybdenum disulfide transistors: an insight into current flow across schottky barriers, ACS Nano 8 (1) (2014) 1031–1038.

[11] M.S. Choi, G.-H. Lee, Y.-J. Yu, D.-Y. Lee, S.H. Lee, P. Kim, J. Hone, W.J. Yoo, Controlled charge trapping by molybdenum disulphide and graphene in ultrathin heterostructured memory devices, Nat. Commun. 4 (1) (2013) 1–7.

[12] C. Qin, Y. Gao, L. Zhang, X. Liang, W. He, G. Zhang, R. Chen, J. Hu, L. Xiao, S. Jia, Flexible engineering of light emission in monolayer mos2 via direct laser writing for multimode optical recording, AIP Adv. 10 (4) (2020), 045230.

[13] W. Huang, H. Da, G. Liang, Thermoelectric performance of mx2 (m= mo, w; x= s, se) monolayers, J. Appl. Phys. 113 (10) (2013), 104304.

[14] M. Amani, M.L. Chin, A.G. Birdwell, T.P. O'Regan, S. Najmaei, Z. Liu, P.M. Ajayan, J. Lou, M. Dubey, Electrical performance of monolayer mos2 field-effect transistors prepared by chemical vapor deposition, Appl. Phys. Lett. 102 (19) (2013), 193107.

[15] A. Pospischil, M.M. Furchi, T. Mueller, Solar-energy conversion and light emission in an atomic monolayer p-n diode, Nat. Nanotechnol. 9 (4) (2014) 257–261.

[16] V.O. Özcelik, J.G. Azadani, C. Yang, S.J. Koester, T. Low, Band alignment of two-dimensional semiconductors for designing heterostructures with momentum space matching, Phys. Rev. B 94 (3) (2016), 035125.

[17] H.-P. Komsa, J. Kotakoski, S. Kurasch, O. Lehtinen, U. Kaiser, A.V. Krasheninnikov, Two-dimensional transition metal dichalcogenides under electron irradiation: defect production and doping, Phys. Rev. Lett. 109 (3) (2012), 035503.

[18] A.H. Reshak, S. Auluck, Theoretical investigation of the electronic and optical properties of zrx2 (x= s, se and te), Phys. B: Condens. Matter 353 (3–4) (2004) 230–237.

[19] Y. Ding, Y. Wang, J. Ni, L. Shi, S. Shi, W. Tang, First principles study of structural, vibrational and electronic properties of graphene-like mx2 (m= mo, nb, w, ta; x= s, se, te) monolayers, Phys. B: Condens. Matter 406 (11) (2011) 2254–2260.

[20] R.J. Toh, Z. Sofer, M. Pumera, Catalytic properties of group 4 transition metal dichalcogenides (mx 2; m= ti, zr, hf; x= s, se, te), J. Mater. Chem. A 4 (47) (2016) 18322–18334.

[21] A.-Y. Lu, H. Zhu, J. Xiao, C.-P. Chuu, Y. Han, M.-H. Chiu, C.-C. Cheng, C.-W. Yang, K.-H. Wei, Y. Yang, et al., Janus monolayers of transition metal dichalcogenides, Nat. Nanotechnol. 12 (8) (2017) 744–749.

[22] J. Zhang, S. Jia, I. Kholmanov, L. Dong, D. Er, W. Chen, H. Guo, Z. Jin, V.B. Shenoy, L. Shi, et al., Janus monolayer transition-metal dichalcogenides, ACS Nano 11 (8) (2017) 8192–8198.

[23] W. Shi, Z. Wang, Mechanical and electronic properties of janus monolayer transition metal dichalcogenides, J. Phys.: Condens. Matter 30 (21) (2018), 215301.

[24] S.-D. Guo, Phonon transport in janus monolayer mosse: a first-principles study, Phys. Chem. Chem. Phys. 20 (10) (2018) 7236–7242.

[25] M. Yagmurcukardes, C. Sevik, F. Peeters, Electronic, vibrational, elastic, and piezoelectric properties of monolayer janus moste phases: a first-principles study, Phys. Rev. B 100 (4) (2019), 045415.

[26] A.E. Mikkelsen, F.T. Bölle, K.S. Thygesen, T. Vegge, I.E. Castelli, Band structure of moste janus nanotubes, Phys. Rev. Mater. 5 (1) (2021), 014002.

[27] L. Ju, M. Bie, X. Tang, J. Shang, L. Kou, Janus wsse monolayer: an excellent photocatalyst for overall water splitting, ACS Appl. Mater. Interfaces 12 (26) (2020) 29335–29343.

[28] M.M. Petrić, M. Kremser, M. Barbone, Y. Qin, Y. Sayyad, Y. Shen, S. Tongay, J. J. Finley, A.R. Botello-Méndez, K. Müller, Raman spectrum of janus transition metal dichalcogenide monolayers wsse and mosse, Phys. Rev. B 103 (3) (2021), 035414.

[29] A. Patel, D. Singh, Y. Sonvane, P. Thakor, R. Ahuja, High thermoelectric performance in two-dimensional janus monolayer material ws-x (x= se and te), ACS Appl. Mater. Interfaces 12 (41) (2020) 46212–46219.

[30] Y. Sun, Z. Shuai, D. Wang, Janus monolayer of wsete, a new structural phase transition material driven by electrostatic gating, Nanoscale 10 (46) (2018) 21629–21633.

[31] E.A. Moujaes, W. Diery, Thermoelectric properties of 1 t monolayer pristine and janus pd dichalcogenides, J. Phys.: Condens. Matter 31 (45) (2019), 455502.

[32] Y. Zhou, X. Yang, Two-dimensional pentagonal janus structures with strong visible light absorption for photovoltaic and photocatalytic applications, Vacuum 181 (2020), 109649.

[33] W.-L. Tao, J.-Q. Lan, C.-E. Hu, Y. Cheng, J. Zhu, H.-Y. Geng, Thermoelectric properties of janus mxy (m= pd, pt; x, y= s, se, te) transition-metal dichalcogenide monolayers from first principles, J. Appl. Phys. 127 (3) (2020), 035101.

[34] Y. Chen, S. Huang, X. Ji, K. Adepalli, K. Yin, X. Ling, X. Wang, J. Xue, M. Dresselhaus, J. Kong, et al., Tuning electronic structure of single layer mos2 through defect and interface engineering, ACS Nano 12 (3) (2018) 2569–2579.

[35] R.A.B. Villaos, C.P. Crisostomo, Z.-Q. Huang, S.-M. Huang, A.A.B. Padama, M. A. Albao, H. Lin, F.-C. Chuang, Thickness dependent electronic properties of pt dichalcogenides, npj 2D Mater. Appl. 3 (1) (2019) 1–8.

[36] H.J. Conley, B. Wang, J.I. Ziegler, R.F. Haglund Jr., S.T. Pantelides, K.I. Bolotin, Bandgap engineering of strained monolayer and bilayer mos2, Nano Lett. 13 (8) (2013) 3626–3630.

[37] P. Lu, X. Wu, W. Guo, X.C. Zeng, Strain-dependent electronic and magnetic properties of mos 2 monolayer, bilayer, nanoribbons and nanotubes, Phys. Chem. Chem. Phys. 14 (37) (2012) 13035–13040.

[38] H. Pan, Y.-W. Zhang, Edge-dependent structural, electronic and magnetic properties of mos 2 nanoribbons, J. Mater. Chem. 22 (15) (2012) 7280–7290.

[39] A. Castellanos-Gomez, R. Roldán, E. Cappelluti, M. Buscema, F. Guinea, H.S. van der Zant, G.A. Steele, Local strain engineering in atomically thin mos2, Nano Lett. 13 (11) (2013) 5361–5366.

[40] S. Ahmad, S. Mukherjee, A comparative study of electronic properties of bulk mos2 and its monolayer using dft technique: application of mechanical strain on mos2 monolayer, 2014.

[41] B. Amin, T.P. Kaloni, U. Schwingenschlögl, Strain engineering of ws 2, wse 2, and wte 2, RSC Adv. 4 (65) (2014) 34561–34565.

[42] C.-H. Chang, X. Fan, S.-H. Lin, J.-L. Kuo, Orbital analysis of electronic structure and phonon dispersion in mos 2, mose 2, ws 2, and wse 2 monolayers under strain, Phys. Rev. B 88 (19) (2013), 195420.

[43] F. Carrascoso, R. Frisenda, A. Castellanos-Gomez, Biaxial versus uniaxial strain tuning of single-layer mos2, Nano Mater. Sci. (2021).

[44] L. Zhu, T. Zhang, Z. Sun, J. Li, G. Chen, S.A. Yang, Thermal conductivity of biaxial-strained mos2: sensitive strain dependence and size-dependent reduction rate, Nanotechnology 26 (46) (2015), 465707.

[45] X. Guan, G. Zhu, X. Wei, J. Cao, Tuning the electronic properties of monolayer mos2, mose2 and mosse by applying z-axial strain, Chem. Phys. Lett. 730 (2019) 191–197.

[46] M. Meng, T. Li, S. Li, K. Liu, Ferromagnetism induced by point defect in janus monolayer mosse regulated by strain engineering, J. Phys. D: Appl. Phys. 51 (10) (2018), 105004.

[47] R. Chaurasiya, A. Dixit, R. Pandey, Strain-mediated stability and electronic properties of ws2, janus wsse and wse2 monolayers, Superlattices Microstruct. 122 (2018) 268–279.

[48] R. Chaurasiya, S. Tyagi, N. Singh, S. Auluck, A. Dixit, Enhancing thermoelectric properties of janus wsse monolayer by inducing strain mediated valley degeneracy, J. Alloy. Compd. 855 (2021), 157304.

[49] D.D. Vo, T.V. Vu, S. Al-Qaisi, H.D. Tong, T. Le, C.V. Nguyen, H.V. Phuc, H.L. Luong, H.R. Jappor, M.M. Obeid, et al., Janus monolayer ptsse under external electric field and strain: a first principles study on electronic structure and optical properties, Superlattices Microstruct. 147 (2020), 106683.

[50] S. Ahmad, M. Idrees, F. Khan, C. Nguyen, I. Ahmad, B. Amin, Strain engineering of janus zrsse and hfsse monolayers and zrsse/hfsse van der waals heterostructure, Chem. Phys. Lett. 776 (2021), 138689.

[51] P. Giannozzi, S. Baroni, N. Bonini, M. Calandra, R. Car, C. Cavazzoni, D. Ceresoli, G.L. Chiarotti, M. Cococcioni, I. Dabo, et al., Quantum espresso: a modular and open-source software project for quantum simulations of materials, J. Phys.: Condens. Matter 21 (39) (2009), 395502.

[52] N. Troullier, J.L. Martins, Efficient pseudopotentials for plane-wave calculations, Phys. Rev. B 43 (3) (1991) 1993.

[53] J.P. Perdew, K. Burke, M. Ernzerhof, Generalized gradient approximation made simple, Phys. Rev. Lett. 77 (18) (1996) 3865.

[54] S. Grimme, Semiempirical gga-type density functional constructed with a long-range dispersion correction, J. Comput. Chem. 27 (15) (2006) 1787–1799.

[55] A. Togo, F. Oba, I. Tanaka, First-principles calculations of the ferroelastic transition between rutile-type and cacl 2-type sio 2 at high pressures, Phys. Rev. B 78 (13) (2008), 134106.

[56] D. Bohm, D. Pines, A collective description of electron interactions. i. magnetic interactions, Phys. Rev. 82 (5) (1951) 625.

[57] D. Pines, D. Bohm, A collective description of electron interactions: Ii. collective vs individual particle aspects of the interactions, Phys. Rev. 85 (2) (1952) 338.

[58] D. Bohm, D. Pines, A collective description of electron interactions: Iii. coulomb interactions in a degenerate electron gas, Phys. Rev. 92 (3) (1953) 609.

[59] W.-L. Tao, J.-Q. Lan, C.-E. Hu, Y. Cheng, J. Zhu, H.-Y. Geng, Thermoelectric properties of janus mxy (m = pd, pt; x, y = s, se, te) transition-metal dichalcogenide monolayers from first principles, J. Appl. Phys. 127 (3) (2020), 035101.

[60] A.C. Neto, F. Guinea, N.M. Peres, K.S. Novoselov, A.K. Geim, The electronic properties of graphene, Rev. Mod. Phys. 81 (1) (2009) 109.
[61] C.-L. Li, New position of dirac points in the strained graphene reciprocal lattice, AIP Adv. 4 (8) (2014), 087119.
[62] N. Fatahi, D. Hoat, A. Laref, S. Amirian, A. Reshak, M. Naseri, 2d hexagonal snte monolayer: a quasi direct band gap semiconductor with strain sensitive electronic and optical properties, Eur. Phys. J. B 93 (2) (2020) 1–7.
[63] W. Zhang, C. Chai, Q. Fan, Y. Song, Y. Yang, Direct and quasi-direct band gap silicon allotropes with low energy and strong absorption in the visible for photovoltaic applications, Results Phys. 18 (2020), 103271, https://doi.org/10.1016/j.rinp.2020.103271. ⟨https://www.sciencedirect.com/science/article/pii/S2211379720317381⟩.
[64] J. Bera, S. Sahu, Strain induced valley degeneracy: a route to the enhancement of thermoelectric properties of monolayer ws 2, RSC Adv. 9 (43) (2019) 25216–25224.
[65] P. Miró, M. Ghorbani-Asl, T. Heine, Two dimensional materials beyond mos2: noble-transition-metal dichalcogenides, Angew. Chem. Int. Ed. 53 (11) (2014) 3015–3018.
[66] S.-D. Guo, X.-S. Guo, R.-Y. Han, Y. Deng, Predicted janus snsse monolayer: a comprehensive first-principles study, Phys. Chem. Chem. Phys. 21 (44) (2019) 24620–24628.
[67] S.-D. Guo, J. Dong, Biaxial strain tuned electronic structures and power factor in janus transition metal dichalchogenide monolayers, Semicond. Sci. Technol. 33 (8) (2018), 085003.
[68] R.C. Andrew, R.E. Mapasha, A.M. Ukpong, N. Chetty, Mechanical properties of graphene and boronitrene, Phys. Rev. B 85 (12) (2012), 125428.
[69] A. Benassi, A. Ferreti, C. Cavazzoni, PWSCFsepsilon.xusersmanual, 2017. ⟨https://ir.library.dc-uoit.ca/bitstream/10155/159/3/McNelles_Phillip_appendixA.pdf⟩.